Supporting Information

DOI:10.1039/C6TA03221D

Green Manufacturing of Metallic Nanoparticles: a Facile and Universal Approach to Scaling up

Jicheng Feng,[a]* Xiaoai Guo,[b] Nabil Ramlawi,[a] Tobias V. Pfeiffer,[a] Ruben Geutjens,[a] Shibabrata Basak,[c] Hermann Nirschl,[b] George Biskos,[a, d, e]* Henny W. Zandbergen,[c] Andreas Schmidt-Ott[a]*

Table of contents:

*to whom correspondence should be addressed to: jic.feng@gmail.com; g.biskos@cyi.ac.cy; a.schmidt-ott@tudelft.nl

DOI:10.1039/C6TA03221D

S1. Applications of the spark produced nanoparticles (NPs)

Table S1 Representative applications of spark produced NPs (operating frequencies < 1 kHz)

Nanomaterials	Reference(s)	Applications	Notes
Mg-Ti	1	H_2 storage	alloy NPs
Pd-Au	2	optical H_2 sensing	nanoparticulate films
Au	3	water splitting	plasmonic effect
Ag	4	solar cells	nanoparticle film
Cu	5	catalysis	catalyzing Ag deposition on a polymer substrate
Pd-Ag, Pt-Ag, Au-Ag	6	catalysis	bimetallic nanostructures for catalytic CO conversion
TiO_2/Graphite oxide	7	photocatalysis	nanocomposites for photocatalytic hydrogenation
Ag	8	spectroscopic	nano dots and nano rings
Ag	9,10	antibacterial	bioaerosol filtration
Au	11–13	growing nanowires	nano seeds
Pd (Cu)/graphene	14	synthesizing core-shell NPs	metal core, multilayer graphene shell
Au/Ag	15	synthesizing core-shell NPs	Au-core, Ag shell; Au nano-seed injected into Ag precursor solution
Au/Ag, Au/polystyrene latex	16	synthesizing core-shell NPs	coagulational deposition
TiO_2	17	perovskite solar cells	creating 3D patterned nanostructures

S2. Comparison the RLCS with the HFS

Figure S1 shows a simple RLC spark (RLCS) circuit and a newly developed switching circuit that decouples charge and discharge cycles by adding a number of fast electronic switches. In the RLCS, the capacitors are charged by a constant current supply. A spark discharge between the two electrodes is formed when the voltage over the capacitor reaches the breakdown voltage. After this discharge, the charging of the capacitor starts again and this process repeats itself at a certain frequency.

By contrast, the HFS separates charge and discharge in the RLC circuit and the sparks are superimposed onto a continuous low glow current between consecutive sparks.[18] This glow current is three orders of magnitude lower compared to that needed to sustain an arc.[19] As a result, it does not result in the ablation of a significant amount of mass from the electrodes[20] and guarantees that the plasma between the electrodes does not extinguish completely between two successive sparks. The applied voltage required for igniting each spark discharge is also kept low because of this current. The spark energy is proportional to the capacitance

DOI:10.1039/C6TA03221D

and to the square of the discharge voltage. Considering that the HFS has a fixed capacitance and applies a constant voltage, constant and low spark energy can thus be well maintained for each spark.[21–23] By keeping a low and constant spark energy and simply increasing the spark repetition frequency, it is easy to linearly increase the NP mass production rate.

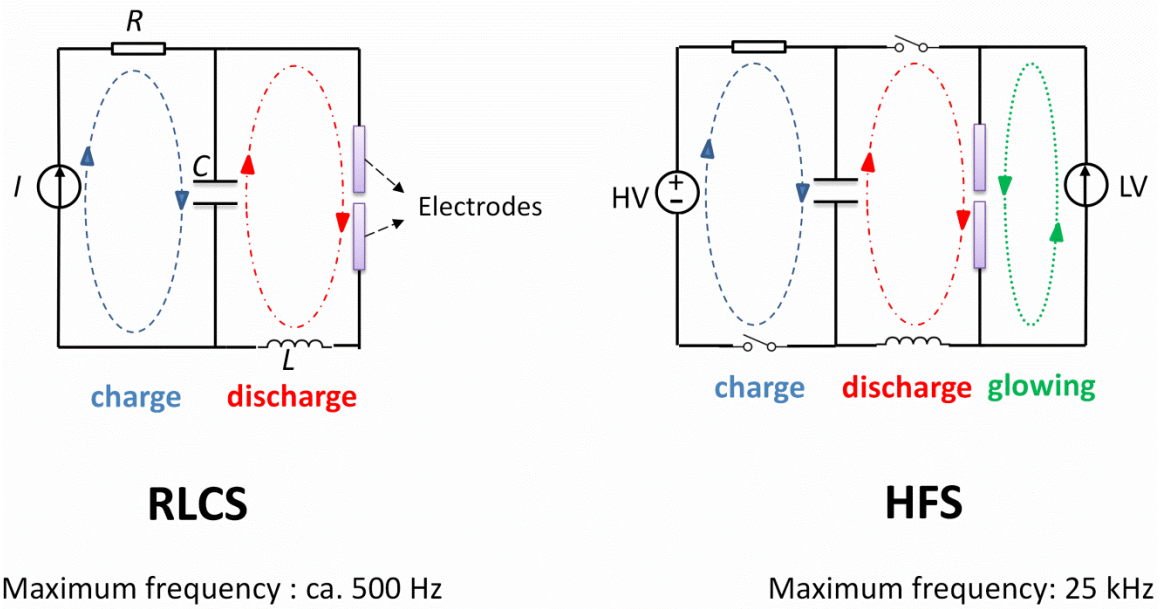

Figure S1. Schematic representation of RLC spark circuit (RLCS) and the high frequency sparks (HFS; i.e., a switching spark circuit) decoupling charge and discharge cycles. Current paths during charge and discharge processes as well as for the continuous glow current are presented by the dashed cycles of different colours (dark blue: charge; red: discharge; green: glow current).

S3. Experimental

Figure S2 shows the schematic layout of the experimental setup that is used to investigate the mass production rate of NPs. It consists of a NP production system (i.e., a spark discharge generator; SDG), online measurement system (i.e., a scanning mobility particle sizer[24]; SMPS), and collection systems (i.e., a filter, and a mini-particle sampler;[25] MPS). The SDG consists of a pair of electrodes connected to a newly developed HFS. The SMPS system[22] constitutes an ^{241}Am bipolar charger, a custom-made differential mobility analyzer (DMA), and a condensation particle counter (CPC; TSI Model 3775). [24]

S3.1 NP production: SDG

The SDG consists of a pair of electrodes connected to a newly developed HFS.[21] The HFS can achieve a spark repetition frequency up to 25 kHz. In contrast to the RLCS,[23] the HFS with a fixed capacitance C_{ca} of 45 nF decouples charge and discharge cycles.[21] Doing so in the HFS allows the applied voltage U_C between the electrodes to be set independent of the breakdown

DOI:10.1039/C6TA03221D

voltage. A low current source in the switch circuit provides a continuous low current in the discharge gap. The continuous low-power discharge within the gap reduces the breakdown voltage of the carrier gas, allowing stable operation at U_C = 1.2 kV for gap distances up to 2 mm. For all the experiments, the energy per spark was fixed to 32.4 mJ (estimated by $E = 0.5\ C_{ca}U_C^2$).

In order to obtain the spark repetition frequency and monitor the spark oscillation, an oscilloscope (HAMEG instruments GmbH, HMO1024) was connected to the HFS using 1:100 HV probes (Testec HV250).

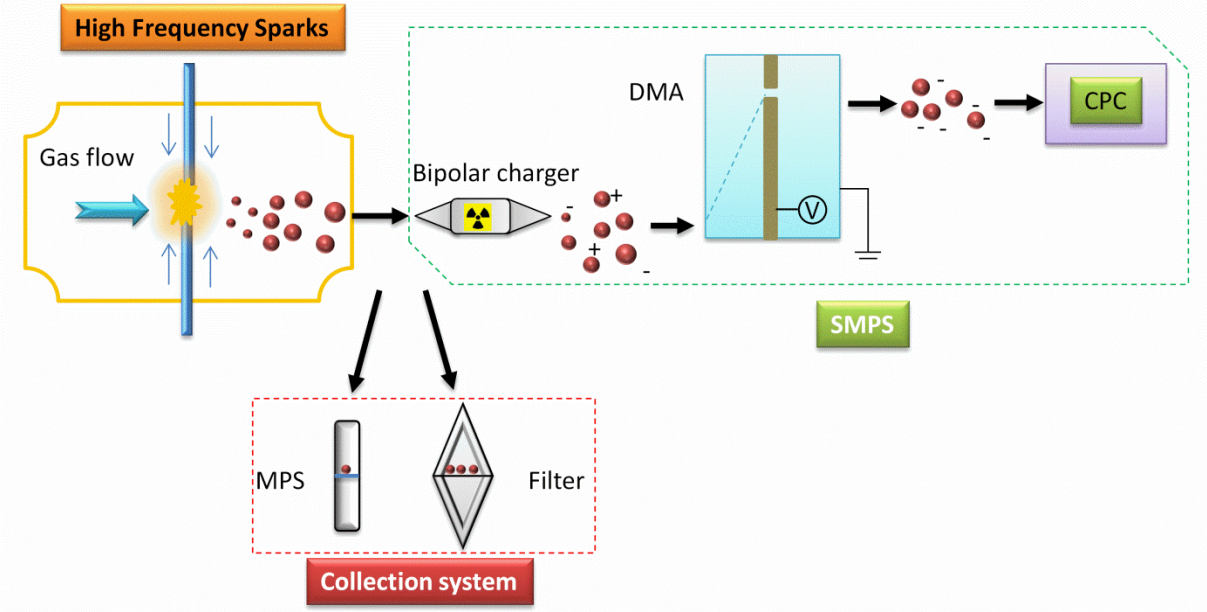

Figure S2. Schematic layout of the experimental setup. Key: DMA, differential mobility analyser; CPC, condensation particle counter; MPS, mini-particle sampler.

S3.2 Experimental materials

The spark discharge generator has been used with pairs of solid electrodes made of Au, Al, Cu, Ag, Ni, Cu-Ni (95-5 at. %), or Zn (all of them have 99.99% purity) having a diameter of 3 mm and a length of 25 mm (MaTecK GmbH) as shown in Figure S2. In all cases, the two electrodes were facing each other with a gap length variable up to 2 mm. A continuous inert gas (Ar, purity 99.999%) flushes through the gap at a rate of 13 standard litres per minute (slm) and a coaxial flow rate of 7 slm (cf. indicated by four blue arrows around the pair of electrodes).

S3.3 Online measurement system: SMPS

An SMPS was used to measure the size distribution of the NPs produced by the HFSs.[26] The system consists of an aerosol charge neutralizer, a differential mobility analyser (DMA) and a

DOI:10.1039/C6TA03221D

condensation particle counter (CPC). The neutralizer located upstream of the DMA brings the particles into a charge equilibrium.[27] The DMA operated with a closed-loop sheath flow system classifies particles based on their electrical mobility. Subsequently, the CPC gives particle concentrations up to 10^7 cm^{-3}.

S3.4 Collection systems for offline characterization

The samples from the collection systems are characterized by transmission electron microscope (TEM; JEOL JEM-1400, and Philips CM12, and FEI Monochromated Tecnai 200STEM-FEG), and a custom-built small- and wide-angle X-ray scattering (SAXS/WAXS) laboratory camera.[28] TEM measurements provide the information of particle morphologies. The MPS was used to collect NPs onto the TEM grids (S143-3 Q'foil 1.2/1.3 400 Cu) with holes, through which the aerosol flow passes, and some particles are collected.[25] The non-destructive SAXS/WAXS technique allows simultaneous measurements of the primary particle, as well as quantitative determination of the crystallite properties, such as the co-existence of crystal phases, and their fractions.[28,29] The samples for SAXS/WAXS were collected on membrane filters (HVHP09050 Durapore PVDF with 0.45 µm pore size and 90 mm in diameter) using a custom-made filter holder.[30] The scattering intensity of the deposited particles is measured as a function of scattering angle 2θ or scattering vector $q = (4\pi/\lambda)\sin\theta$, where λ is the wavelength of X-ray beam (λ = 0.154 nm).

S4. Mass ablated per spark

Table S2. Physical constants of the applied electrode materials and Δm

Materials	Density (g/cm^3)	H_e (J/kg)	H_m (J/kg)	T_b (K)	T_m (K)	C_{ps} (J/(K kg))	Δm (mg)
Zn	7.14	1.8×10^6	1.1×10^5	1180	693	392	6.6×10^{-6}
Ag	10.49	2.4×10^6	1.0×10^5	2435	1235	234	4.9×10^{-6}
Al	2.70	1.1×10^7	4.0×10^5	2743	933	896	2.4×10^{-6}
Cu	8.96	4.7×10^6	2.1×10^5	2835	1358	382	3.6×10^{-6}
Au	19.30	1.7×10^6	6.4×10^4	3243	1337	129	13×10^{-6}
Ni	8.91	6.4×10^6	1.7×10^4	3003	1728	442	2.5×10^{-6}

Here, Δm represents the slope of the linear fittings to the measurements as shown in Figure 1 of the main manuscript.

The mass ablated per spark can be estimated by the evaporation model expressed as:[31]

$$\Delta m \approx \frac{\alpha E}{c_{ps}(T_b - T) + H_m + H_e} \quad \text{(S1)}$$

DOI:10.1039/C6TA03221D

Here, E is the energy per spark (J); α is the fraction of spark energy consumed for particle production, which can be empirically estimated to be in the order of ca. 0.1 %;[32] c_{ps} (J K^{-1} kg^{-1}) is the heat capacity of the solid material; T and T_b are the room temperature, and the boiling point of the materials, respectively; H_m and H_e (J kg^{-1}) are the enthalpies of melting and vaporization of the materials. Values of the properties of all material used in this study are given in Table S2.

S5. Design of recycling flow system

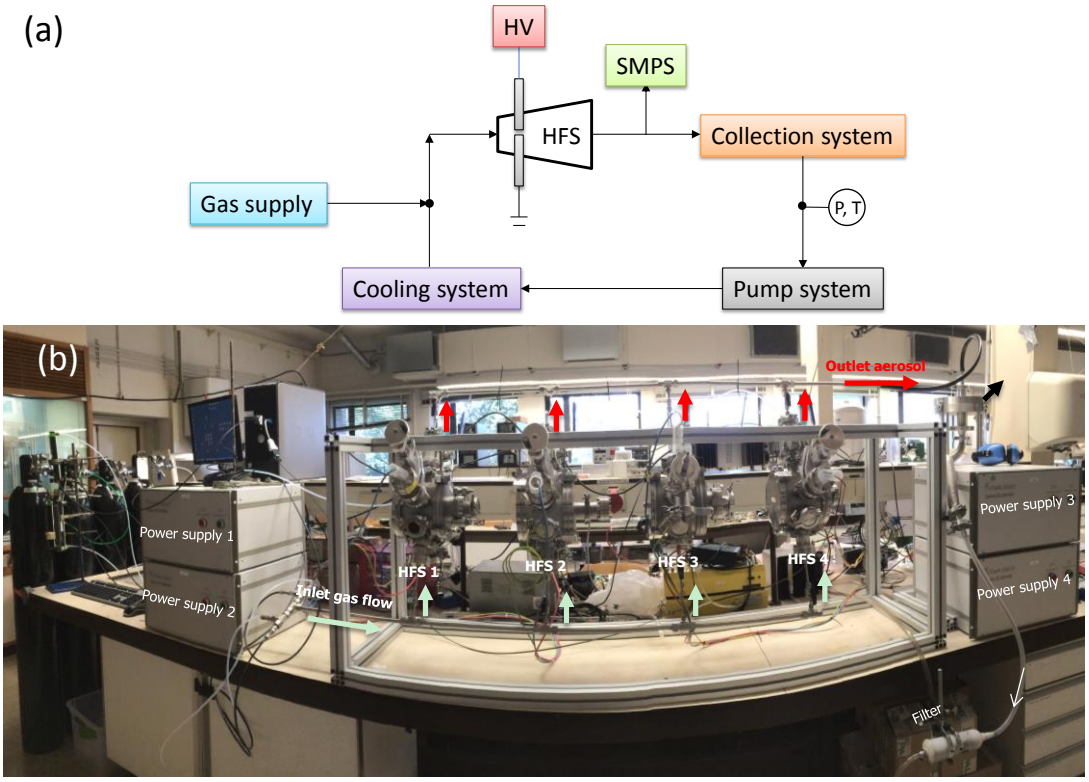

Figure S3. Schematic layout of the recycling flow system (a) and the photograph of the multiple HFSs (four unites here) for producing NPs (b). In principle the multiple HFSs can also be operated in such configuration.

Figure S3a depicts the recycling flow system in the HFS for NP production, which can be capable of handling a high flow rate of ca. 500 slm. A gas supply is placed upstream of the HFS. This gas quenches the spark and carries away the aerosol NPs to the collection system. Pressure and temperature of the gas are monitored. The pump system drives the flow and also defines the flow rate. A cooling system is used to remove heat generated by the pump system and the HFS. In addition, there is an outlet for online measurement of the produced NPs. In principle, this recycling flow system is also working for multiple HFSs that deliver the NPs on an industrial scale. In order to show the multiple HFSs, we provide a photograph for four

DOI:10.1039/C6TA03221D

units of them. Further numbering up should be available, depending on the demands from the end-users.

S6. Electrode gap control system

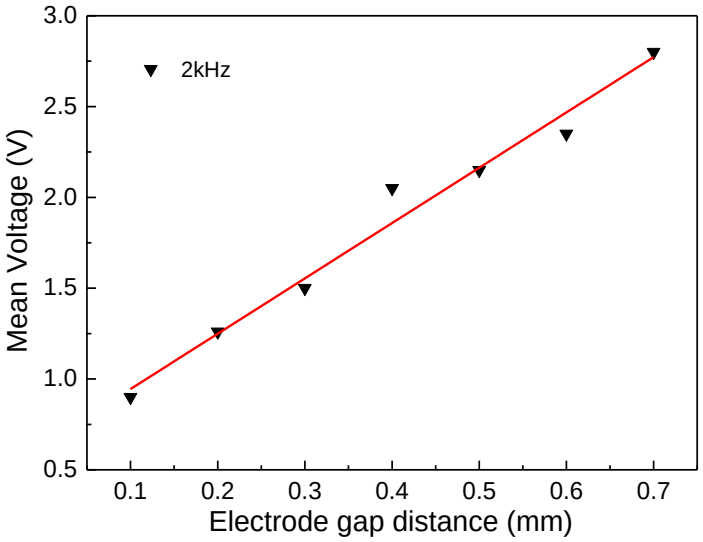

Figure S4. Mean gap voltage V_{mean} of the glow current as a function of gap distance between two Al electrodes in Ar at the spark frequency of 2 kHz. The measurements (points) are matched with the line.

Figure S4 shows that the mean gap voltage of the glow current between successive sparks is linearly dependent on the gap distance. A custom-made electrical device (cf. Figure S5) is applied to derive the control signal V_{mean} from the voltage U_{gap} across the sparks. It forms the difference between the potentials of the electrodes and integrates the potentials over the time to form the averaged values. Consequently, the electrode gap can be monitored by V_{mean} that varies monotonically with the gap distance as shown in equation (S4).

In order to enable continuous and stable operation of HFS, a robust electrode feeder system needs to be designed. For example, when the HFS is operated at 25 kHz, the consumption rate of Au solid electrodes with a diameter of 3 mm is estimated to be 8 mm/h. Such a rapid electrode consumption rate leads to discontinuous production mode since the gap distance for a stable spark lies only below ca. 2 mm for a given voltage of 1.2 kV in the HFS.

DOI:10.1039/C6TA03221D

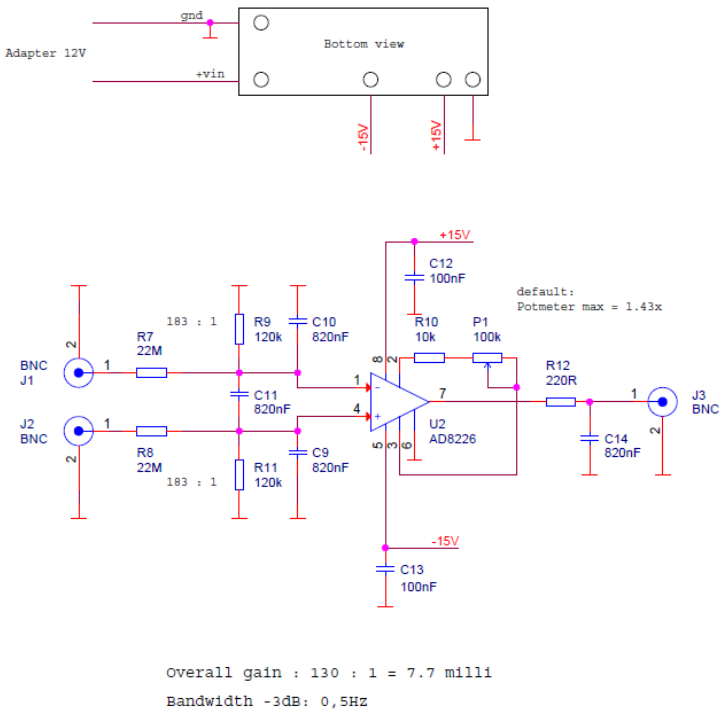

Figure S5. Differential amplifier measuring the mean (time averaged) gap voltage. The amplifier gain is set to 130:1. Maximum output voltage is ±15 V. The bandwidth is 0.5 Hz.

Considering that a constant voltage U_c over the electrodes has been applied in our HFS, it is not feasible to control the gap distance from a direct measurement of this voltage signal as the RLCS does. In addition, the spark resistance R_s is independent of the gap distance.[33] This means that the peak current $I_{peak} = U_c/R_s$ is also constant. As a result, both the voltage and peak current cannot be used to control the gap distance. The resistance of the glow current R_{GC} (cf. Figure S1) between the successive sparks can be expressed as:

$$R_{GC} \propto \frac{d_{gap}}{A_{cs}} \tag{S2}$$

where A_{cs} is the cross sectional area of the glow current, and d_{gap} is the electrode gap distance. The gap voltage U_{gap} must also depend on d_{gap}, which can be written as:

$$U_{gap} \propto \frac{I}{A_{cs}} d_{gap} \tag{S3}$$

where I is the glow current between two successive sparks, and I/A_{cs} is the glow current density, which can be assumed as a constant.[33] Therefore, equation (S3) can be simplified to:

$$U_{gap} \propto d_{gap} \tag{S4}$$

This linear relation is further confirmed by our measurements shown in Figure S4.

DOI:10.1039/C6TA03221D

S7. The mass production rate estimated by the size distribution of the particles

A scaling relation describing an agglomerate with a mobility diameter d_{mb} consisting of primary particles having a mean size d_{pp} is given by:[34]

$$\frac{M_{\mathrm{ag}}(d_{\mathrm{mb}})}{m_{\mathrm{pp}}} = C_1 \left(\frac{d_{\mathrm{mb}}}{d_{\mathrm{pp}}}\right)^{D_{\mathrm{f}}} N_{\mathrm{ag}}(d_{\mathrm{mb}}) \tag{S5}$$

where C_1 can be approximated with unity;[35] D_{f} is the mass-mobility exponent;[36] m_{pp} is the mass of one primary particle, and $M_{\mathrm{ag}}(d_{\mathrm{mb}})$ and $N_{\mathrm{ag}}(d_{\mathrm{mb}})$ are the mass density and the number concentration of the agglomerates as a function of a mobility diameter d_{mb}. Assuming that the primary particles have the density of the bulk material ρ, the sum of the mass of agglomerates M_{ag} is given by:

$$M_{\mathrm{ag}} = \rho \frac{\pi}{6} {d_{\mathrm{pp}}}^3 \int_0^{\infty} \left(\frac{d_{\mathrm{mb}}}{d_{\mathrm{pp}}}\right)^{D_{\mathrm{f}}} \frac{\mathrm{d}N_{\mathrm{ag}}(d_{\mathrm{mb}})}{\mathrm{d}d_{\mathrm{mb}}} \mathrm{d}d_{\mathrm{mb}} \tag{S6}$$

Assuming that D_{f} is a constant for a specific size distribution and a constant d_{pp}, the size distribution of the aerosol NPs can always be fitted to a lognormal function with a total particle number concentration N_{tot}, a geometry mean diameter d_{pm}, and a geometric standard deviation σ_{g}.[37] Therefore, the solution of equation (S6) is given by:

$$M_{\mathrm{ag}} = \frac{\pi}{6} \rho {d_{\mathrm{pp}}}^{3-D_{\mathrm{f}}} N_{\mathrm{tot}} \exp\left(\frac{{D_{\mathrm{f}}}^2 \left(\ln\sigma_{\mathrm{g}}\right)^2}{2}\right) (d_{\mathrm{pm}})^{D_{\mathrm{f}}} \tag{S7}$$

Assuming particle losses are negligible during aerosol NP transport, the mass production rate $\dot{m}$ can be expressed as:

$$\dot{m} = M_{\mathrm{ag}} Q \tag{S8}$$

Substituting equation (S7) to equation (S8), one can obtain:

$$\dot{m} = \frac{\pi}{6} Q \rho {d_{\mathrm{pp}}}^{3-D_{\mathrm{f}}} N_{\mathrm{tot}} \exp\left(\frac{{D_{\mathrm{f}}}^2 \left(\ln\sigma_{\mathrm{g}}\right)^2}{2}\right) (d_{\mathrm{pm}})^{D_{\mathrm{f}}} \tag{S9}$$

N_{tot}, σ_{g} and d_{pm} are known quantities determined by a log-normal particle size distribution (i.e., SMPS measurements), whereas d_{pp} can be obtained by analysing TEM images or SAXS measurements. The only unknown parameter D_{f} can be estimated by matching equation (S9) to the gravimetric measurements.

The SMPS measurements show that the Ni NPs have the highest concentration among the materials tested in this study (cf. Figure 3a in the main manuscript), while their mass production rate is relatively low (cf. Figure 1 in the main manuscript). This apparent

DOI:10.1039/C6TA03221D

discrepancy can be attributed to the fact that the larger surface area of Ni agglomerates resulting from their smaller primary particles (see Table 2 in the main manuscript) leads to a larger mobility diameter for the same mass per agglomerate. Another likely reason for the larger mobility diameter is that Ni NPs probably tend to form linear chain-like structures (cf. Figure S8a) due to their magnetism.[38] Larger particles results in fewer diffusional losses when transported through the tubing of the experimental setup, explaining its higher concentration.

Table S3. Comparison of the mass production rates $\dot{m}$ estimated on the basis of the size distributions of the particles (i.e., SMPS measurements), and that is determined by the gravimetric measurements at a spark frequency of 1 kHz.

Materials	d_{mp} (nm)	σ_g	N_{tot} (#/cm^3)	D_f	M_{ag} (mg/cm^3)	$\dot{m}$ (mg/h)
Al	56	1.52	6.34×10^7	2.26	0.73×10^{-5}	8.8
Ni	68	1.56	9.68×10^7	1.95	0.78×10^{-5}	9.5
CuNi	48	1.59	5.90×10^7	2.11	0.93×10^{-5}	11.3
Cu	41	1.71	5.36×10^7	2.24	1.09×10^{-5}	13.3
Ag	38	1.72	4.59×10^7	2.37	1.43×10^{-5}	17.5
Zn	51	1.81	4.55×10^7	2.21	1.98×10^{-5}	24.2
Au	--	--	-	-	-	46.5

Table S4. The mass production rate $\dot{m}$ determined by the size distributions of Cu NPs generated at different frequencies ranging from 1.0 to 4.2 kHz

Frequency (kHz)	M_{ag} (mg/cm^3)	$\dot{m}$ (mg/h)	D_f	D_f (15% losses)
1.0	1.09×10^{-5}	13.3	2.24	2.18
1.4	1.50×10^{-5}	18.4	2.35	2.29
1.8	1.95×10^{-5}	23.9	2.35	2.29
2.5	2.70×10^{-5}	32.4	2.44	2.37
3.3	3.32×10^{-5}	41.8	2.44	2.39
4.2	4.38×10^{-5}	53.6	2.47	2.41

Table S4 shows the mass production rate determined by size distributions of Cu NPs produced at different frequencies (from 1.0 to 4.2 kHz). The substantially increased concentrations of agglomerated NPs at higher spark frequency (cf. Figure 3b in the main manuscript) and the value of mass-mobility exponent, which correlates well with previous publications,[36,39] imply that equation (2) in the main manuscript can be used to estimate the mass production rate. The mass-mobility exponent ranges from 2.24 to 2.47 (cf. Table S4). If we assume that particle losses are in the order of 15% during particle transport to the SMPS system, this range changes from 2.18 to 2.41. The values of M_{ag} and the mass-mobility

DOI:10.1039/C6TA03221D

exponent of different materials at 1 kHz (cf. Figure 3a) and Cu NPs at different spark frequencies (cf. Figure 3b) are summarized in Tables S3 and S4.

S8. TEM images of NPs consisting of different materials

Figure S6 shows TEM, HRTEM, STEM images of Au, Zn, Al, Ag, Ni, and Al NPs produced by HFS at the frequency of 1 kHz. The purpose of TEM images of different materials is to show the primary particles within the agglomerates. We can also produce non-agglomerated singlet particles (Au and Ag NPs of HRTEM images and STEM for Ag NPs) and earlier works have reported how to produce these singlets.[23,32] Combining the TEM imaging with the SMPS measurements (cf. Figure 3 in the main manuscript), it is seen that the number concentration profile in the large size range (> 100 nm) is mostly attributed to the agglomerates rather than the splashing particles. The primary particle sizes of both Al and Ni NPs are ca. 5 nm. Note that the primary particle size of Zn NPs is disproportionately large (ca. 15 nm), which can be attributed to its lowest melting point out of the materials tested in this work, indicating a lower solid-state surface diffusion coefficient. Another reason for this is that the larger amount of material ablation makes the effective density of gas-vapour mixture higher (flow rate is the same as other materials), which promotes further coalescence in a hotter initial zone. Moreover, Zn also possesses a larger value of $\Delta m/\rho$ among other materials (cf. Table 1 in the main manuscript).

DOI:10.1039/C6TA03221D

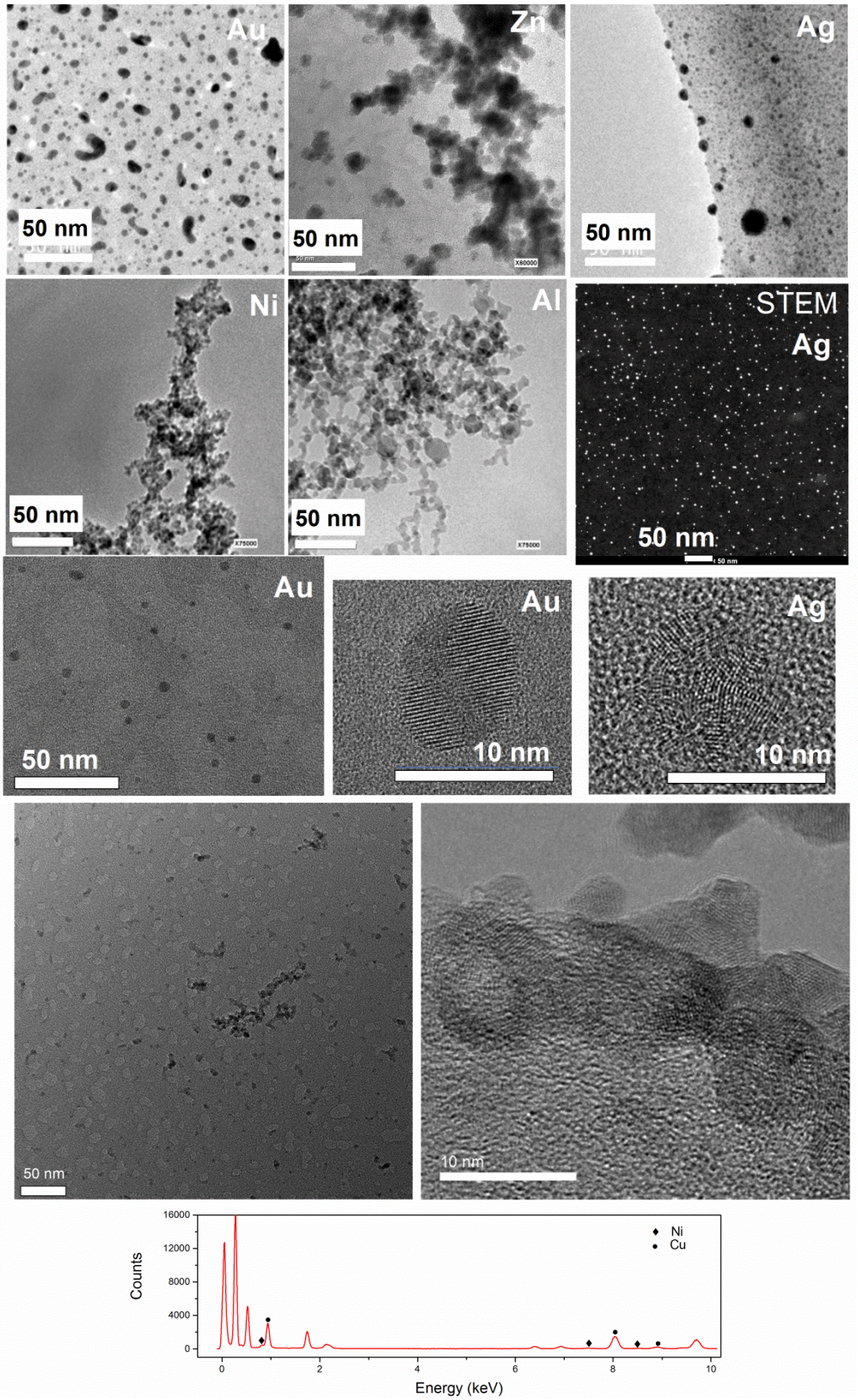

Figure S6. TEM images of Au, Zn, Al, Ag, Ni, and Al NPs generated by HFS at a frequency of 1 kHz. Due to long deposition (i.e., high NP surface coverage on substrates), the agglomerates form on the TEM grid. As a result, the micrographs for Zn, Ni and Al show the small primary particles within the agglomerates. To show the non-agglomerated NPs, we

DOI:10.1039/C6TA03221D

provide the TEM and STEM images for Au and Ag NPs with highly crystalline structure collected in a short time (ca. 1 s, to guarantee a low surface coverage of NPs on substrates). TEM images of CuNi NPs and the associated EDS (assembled at the bottom), showing that the composition of Cu-Ni NPs (97:3) is similar to that of the staring electrodes (95:5), and their crystal structure.

From the micrographs obtained from agglomerates in Figure S6, it can be seen that for the primary particle diameters d_{pp} for Ni, Al and Zn: d_{pp} (Ni) < d_{pp} (Al) < d_{pp} (Zn), corresponding well with the indication of $\Delta m/\rho$, which provides the order of the materials tested in this work: d_{pp} (Cu-Ni) < d_{pp} (Ni) < d_{pp} (Cu) < d_{pp} (Ag) < d_{pp} (Au) < d_{pp} (Al) < d_{pp} (Zn). In the case of Ag and Au, the criteria lead to opposite trends due to the fact that the noble metallic NPs are prone to coalesce after the deposition and the observation of particle coalescence under electron beam of TEM. Concerning the comparison of Cu with CuNi (95-5 at.%) (cf. Table 2 in the main manuscript), both indicators (e.g., $\Delta m/\rho$ and surface diffusion coefficient) are similar, but CuNi exhibits a smaller primary particle size. This may be due to the Ni segregating to the surface and reducing the surface diffusion coefficient. The melting point of a given material can only be considered as a reliable indicator of surface diffusion for single-component NPs.

The non-agglomerated Au and Ag NPs were collected in a short time (ca. 1 s), indicating that the agglomerates are formed on substrates rather than in the gas phase. This makes the deposition of non-agglomerated singlet particle possible. Note that such singlet particles should maintain the low surface coverage. In the case of high surface coverage, we can either rapidly coat the NPs in the gas phase before deposition or drastically decrease the temperature below the threshold one for hindering particle coalescence.

S9. Particle size distributions with a fixed *Q/f*

Figure S7 shows the size distributions of Ag particles at two different spark repetition frequencies and gas flow rates, i.e., by keeping the same ratio *Q/f*. Thus similar particle size distributions are obtained. The slightly low concentration at higher flow rate is due to the fact that the resulting turbulence leads to substantial diffusional losses.[32]

DOI:10.1039/C6TA03221D

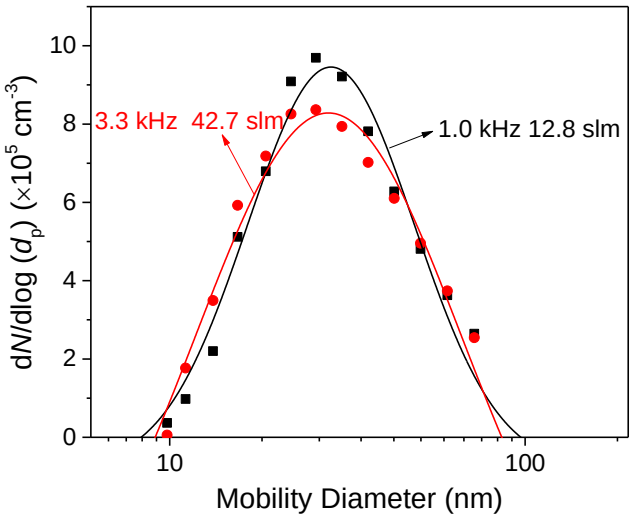

Figure S7. Size distributions of Ag particles at different carrier gas flow rates that linearly increased with the spark repetition frequency.

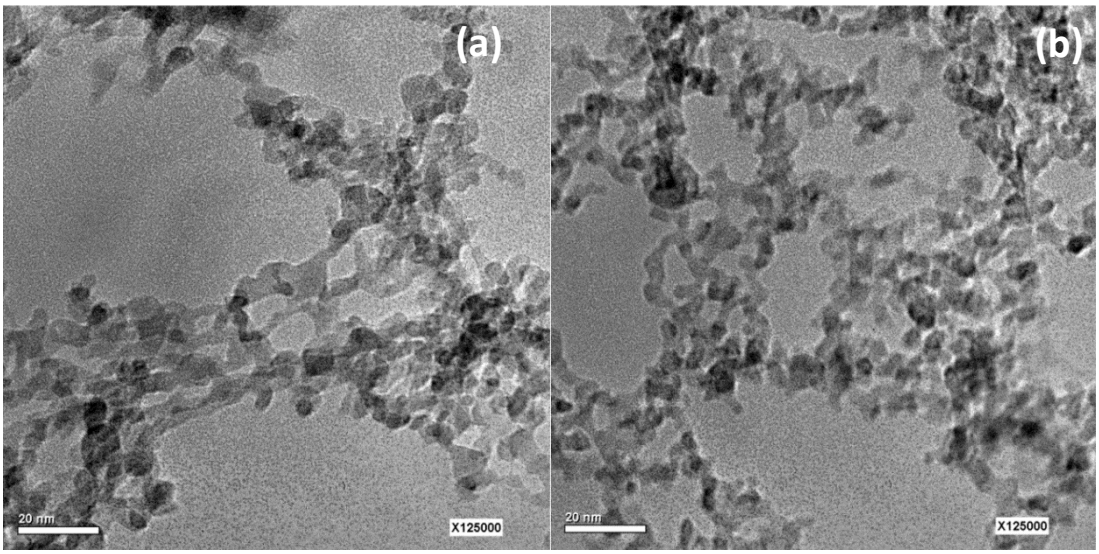

Figure S8. TEM images of Al agglomerates produced by the HFS at f = 2 kHz and Q = 30 slm (a), and at f = 3 kHz and Q = 45 slm (b)

S10. Mass production rate of NPs in dry gas-phase synthesis methods (no liquid precursor)

Table S5 Mass production of NPs in gas-phase synthesis methods

Techniques	Pressure (Pa)	Production rate (g/h)	Particle size (nm)	Material
Plasma[42]	180-1860	0.014-0.052	2-8	Si
Arc discharge[41]	ambient pressure	10	~100	Metals
Spark ablation	ambient pressure	~1 (one electrode pair)	0.5-20 nm	Conducting, semiconducting and mixed NPs

DOI:10.1039/C6TA03221D

In principle, any production rate is feasible, because in contrast to most other methods, spark ablation is easily scalable by simply numbering up the electrode pairs while maintaining consistency in product quality, attributed to good kinetic control in a continuous manner. Scalable methods for high-yield synthesis of particles a few nm in size hardly exist, especially if avoiding any liquid precursors and post-processing is desired. In addition, our method enables the production of thermodynamically metastable materials due to the associated rapid quenching.[32,40] Table S5 compares the nanoparticle production rates of our method with those of other scalable techniques that come close to the size range of our methods. It should be noted that it is much easier to achieve a high production rate for larger particle sizes, which explains the high rates reported for arc discharges.[41] Table S5 does not include flame and laser ablation methods, because the former employs liquid precursors and the latter requires expensive laser sources which inhibit scalability.

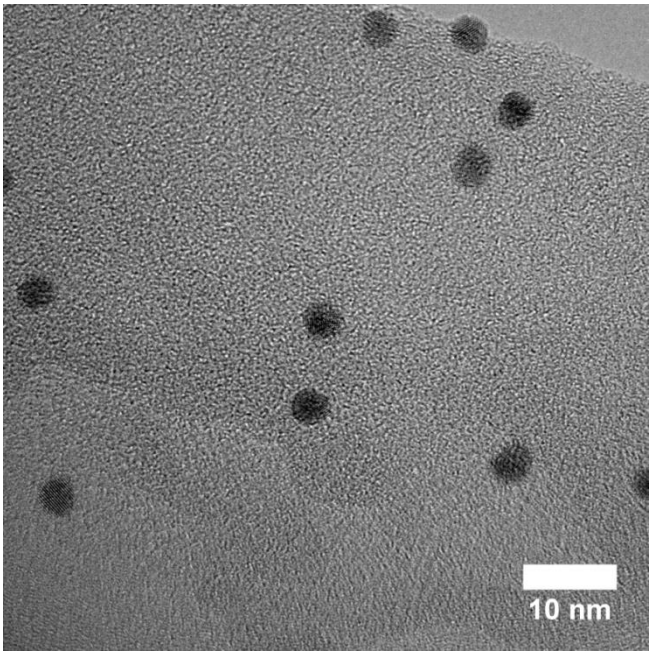

Figure S9. HRTEM image of non-agglomerated Au singlet NPs generated by spark ablation (Q = 50 slm, f = 60 Hz).

Figure S9 again evidences the production of non-agglomerated singlet particles when utilizing an appropriate ratio Q/f in the HFS. On the other hand, the coverage on substrates is also a major determinant for collecting individual singlet particles. This is because high purity singlets strongly coalesce due to collisions, forming the agglomerates. Due to the absence of any liquid chemicals, the prevention of further coalescence is difficult here. However, in combination with insights from the chemists, this should be easily addressed by using some

DOI:10.1039/C6TA03221D

gaseous chemicals, which can form a protecting layer on the particle surfaces, such as coating particles by introducing a trace amount of oxygen in the carrier gas.

S11. SAXS/WAXS measurements for different NPs

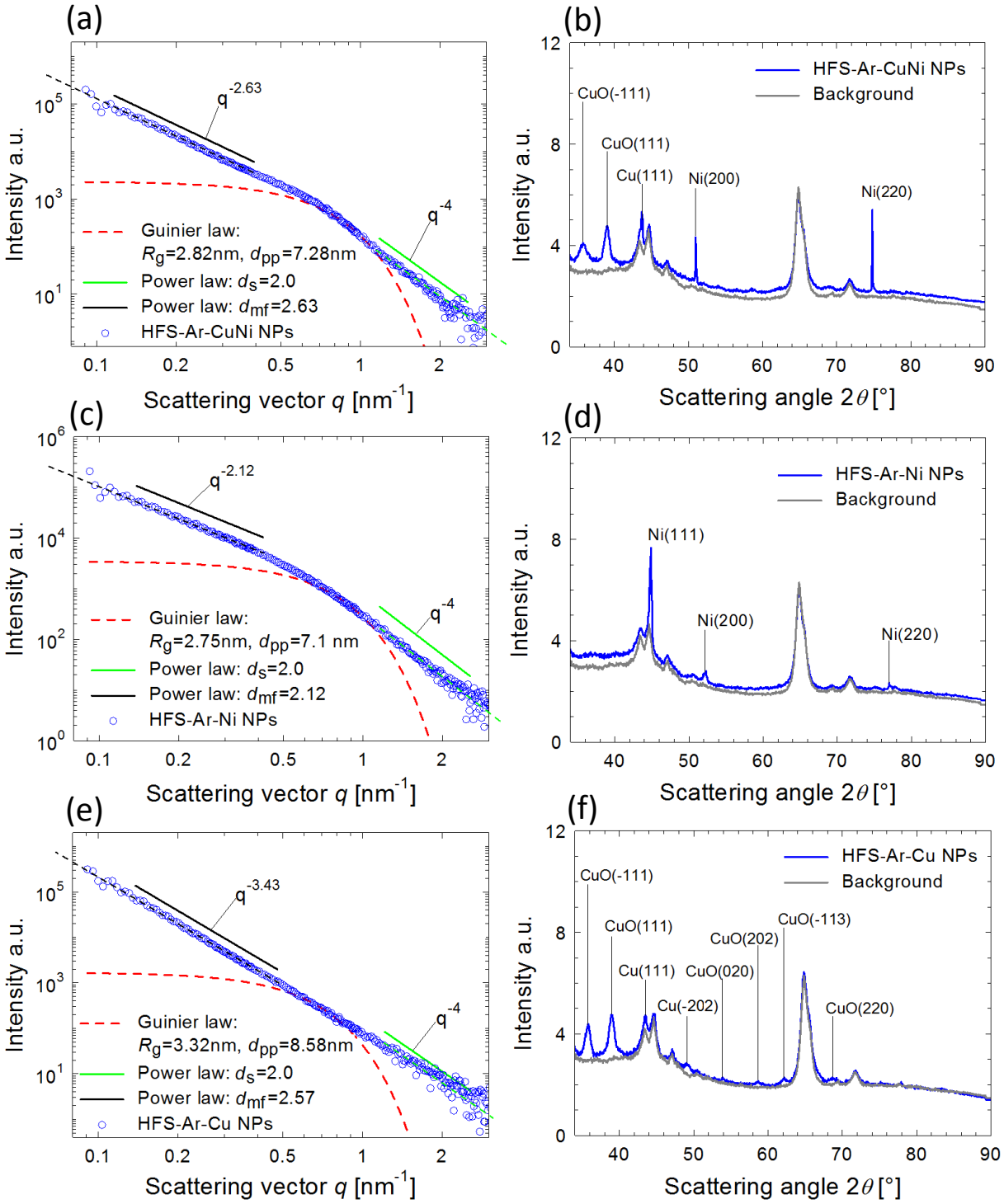

DOI:10.1039/C6TA03221D

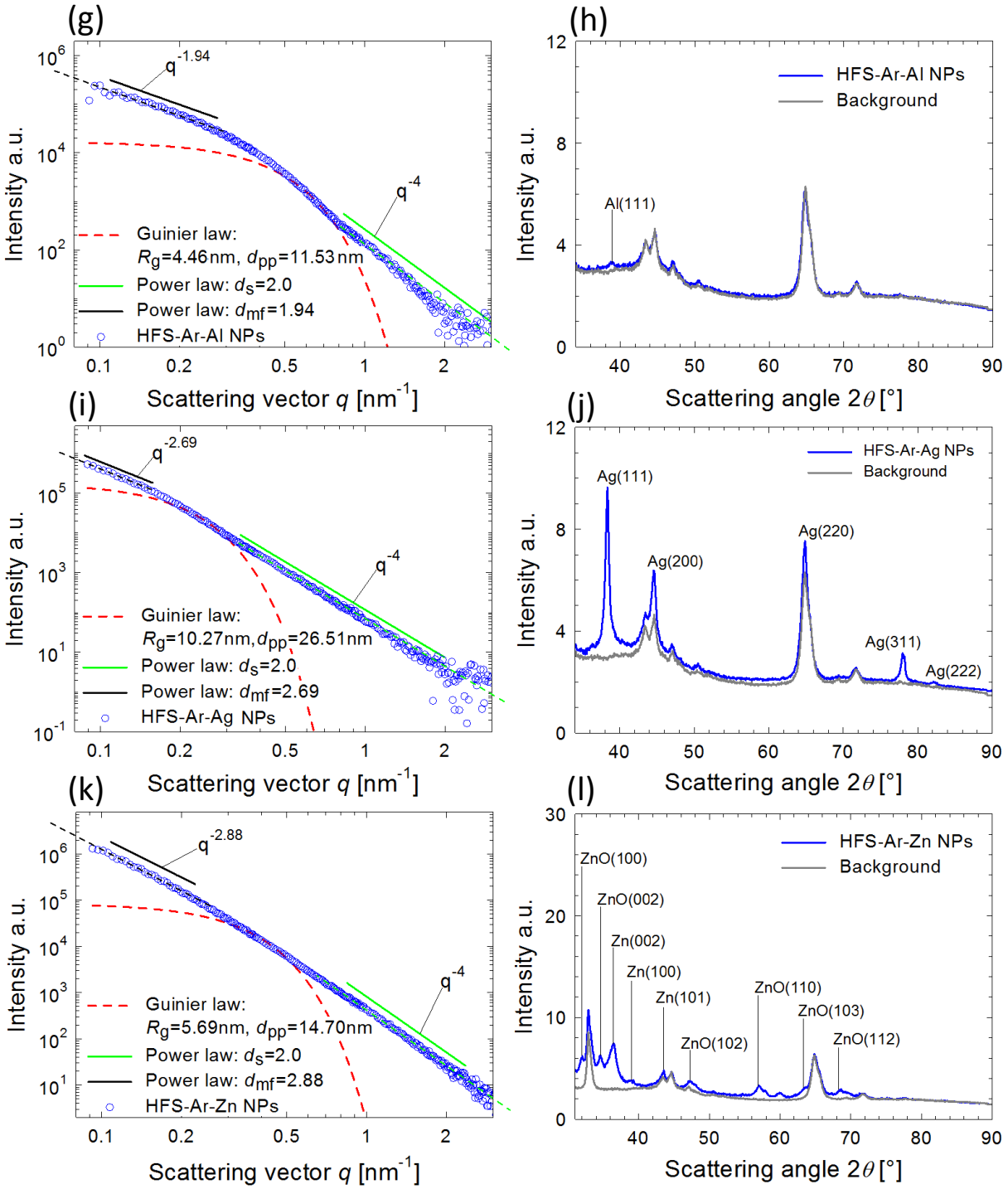

Figure S10. SAXS/WAXS measurements for various NPs. (a, b) CuNi, (c, d) Ni, (e, f) Cu, (g, h) Al, (i, g) Ag, (k, l) Zn. This figure is summarized in Table 2 in the main manuscript.

DOI:10.1039/C6TA03221D

References of the Supporting Information

1 A. Anastasopol, T. V Pfeiffer, J. Middelkoop, U. Lafont, R. J. Canales-Perez, A. Schmidt-Ott, F. M. Mulder and S. W. H. Eijt, *J. Am. Chem. Soc.*, 2013, **135**, 7891–7900.

2 N. A. Isaac, P. Ngene, R. J. Westerwaal, J. Gaury, B. Dam, A. Schmidt-Ott and G. Biskos, *Sensors Actuators B Chem.*, 2015, **221**, 290–296.

3 M. Valenti, D. Dolat, G. Biskos, A. Schmidt-ott and W. A. Smith, *J. Phys. Chem. C*, 2015, **119**, 2096–2104.

4 T. V. Pfeiffer, J. Ortiz-Gonzalez, R. Santbergen, H. Tan, A. Schmidt-Ott, M. Zeman and A. H. M. Smets, *Energy Procedia*, 2014, **60**, 3–12.

5 J. H. Byeon and J. T. Roberts, *ACS Appl. Mater. Interfaces*, 2012, **4**, 2515–20.

6 J. H. Byeon and J.-W. Kim, *ACS Appl. Mater. Interfaces*, 2014, **6**, 3105–3110.

7 J. H. Byeon and J.-W. Kim, *J. Mater. Chem. A*, 2014, **2**, 6939–6944.

8 J. Byeon, D. Park and J. Kim, *Nanoscale*, 2015, **7**, 2271–2275.

9 Y. H. Joe, W. Ju, J. H. Park, Y. H. Yoon and H. Jungho, *Aerosol air quaility Res.*, 2013, **13**, 1009–1018.

10 J. Feng, E. Hontañón, M. Blanes, J. Meyer, X. Guo, L. Santos, L. Paltrinier, N. Ramlawi, L. C. P. M. de Smet, H. Nirschl, F. E. Kruis, A. Schmidt-Ott and G. Biskos, *ACS Appl. Mater. Interfaces*, 2016.

11 M. Heurlin, M. H. Magnusson, D. Lindgren, M. Ek, L. R. Wallenberg, K. Deppert and L. Samuelson, *Nature*, 2012, **492**, 90–94.

12 M. E. Messing, K. A. Dick, L. R. Wallenberg and K. Deppert, *Gold Bull.*, 2009, **42**, 20–26.

13 M. E. Messing, K. Hillerich, J. Bolinsson, K. Storm, J. Johansson, K. A. Dick and K. Deppert, *Nano Res.*, 2010, **3**, 506–519.

14 S. K. Sengar, B. R. Mehta, R. Kumar and V. Singh, *Sci. Rep.*, 2013, **3**, 2814.

15 J. H. Byeon and Y.-W. Kim, *Nanoscale*, 2012, **4**, 6726–6729.

16 T. Pfeiffer, P. Kedia, M. E. Messing, M. Valvo and A. Schmidt-Ott, *Materials (Basel).*, 2015, **8**, 1027–1042.

17 S. Jang, J. Yoon, K. Ha, M. Kim, D. H. Kim, S. M. Kim, S. M. Kang, S. J. Park, H. S. Jung and M. Choi, *Nano Energy*, 2016, **22**, 499–506.

18 WO 2013/115644, 2013.

19 T. V. Pfeiffer, TU Delft, Delft University of Technology, 2014.

20 A. Fridman, *Plasma Chemistry*, Cambridge University Press, Cambridge, 2012.

DOI:10.1039/C6TA03221D

21 T. V. Pfeiffer, J. Feng and A. Schmidt-Ott, *Adv. Powder Technol.*, 2014, **25**, 56–70.

22 N. S. Tabrizi, M. Ullmann, V. A. Vons, U. Lafont and A. Schmidt-Ott, *J. Nanoparticle Res.*, 2009, **11**, 315–332.

23 J. Feng, G. Biskos and A. Schmidt-Ott, *Sci. Rep.*, 2015, **5**, 15788.

24 S. C. Wang and R. C. Flagan, *Aerosol Sci. Technol.*, 1990, **13**, 230–240.

25 B. R'mili, O. L. C. Le Bihan, C. Dutouquet, O. Aguerre-Charriol and E. Frejafon, *Aerosol Sci. Technol.*, 2013, **47**, 767–775.

26 G. Biskos, V. A. Vons, C. U. Yurteri and A. Schmidt-Ott, *KONA Powder Part. J.*, 2008, **26**, 13–35.

27 W. C. Hinds, *Aerosol Technology: Properties, Behavior, and Measurement of Airborne Particles*, John Wiley & Sons, New York, 1999.

28 X. Guo, A. Gutsche and H. Nirschl, *J. Nanoparticle Res.*, 2013, **15**, 2058.

29 X. Guo, M. Wagner, A. Gutsche, J. Meyer, M. Seipenbusch and H. Nirschl, *J. Aerosol Sci.*, 2015, **85**, 17–29.

30 N. S. Tabrizi, *Generation of Nanoparticles by Spark Discharge*, TUDelft, Delft, 2009.

31 F. Llewellyn Jones, *Br. J. Appl. Phys.*, 1950, **1**, 60–65.

32 J. Feng, L. Huang, L. Ludvigsson, M. E. Messing, A. Maisser, G. Biskos and A. Schmidt-Ott, *J. Phys. Chem. C*, 2016, **120**, 621–630.

33 V. Vons, *Spark Discharge Generated Nanoparticles for Hydrogen Storage Applications*, TU Delft, Delft University of Technology, 2008.

34 A. Schmidt-Ott, *J. Aerosol Sci.*, 1988, **19**, 553–563.

35 A. Schmidt-Ott, U. Baltensperger, H. . Gäggeler and D. . Jost, *J. Aerosol Sci.*, 1990, **21**, 711–717.

36 D. Broßell, M. Valenti, S. Bezantakos, A. Schmidt-Ott and G. Biskos, *Aerosol Sci. Technol.*, 2015, **49**, 495–507.

37 J. Heintzenberg, *Aerosol Sci. Technol.*, 1994, **21**, 46–48.

38 S. Lösch, G. N. Iles, B. Schmitz and B. H. Günther, *J. Phys. Conf. Ser.*, 2011, **327**, 012036.

39 C. R. Svensson, L. Ludvigsson, B. O. Meuller, M. L. Eggersdorfer, K. Deppert, M. Bohgard, J. H. Pagels, M. E. Messing and J. Rissler, *J. Aerosol Sci.*, 2015, **87**, 38–52.

40 V. Sebastian, M. Arruebo and J. Santamaria, *Small*, 2014, **10**, 835–853.

41 C. A. Charitidis, P. Georgiou, M. A. Koklioti, A.-F. Trompeta and V. Markakis, *Manuf. Rev.*, 2014, **1**, 1–19.

DOI:10.1039/C6TA03221D

42 L. Mangolini, E. Thimsen and U. Kortshagen, *Nano Lett.*, 2005, **5**, 655–9.